International Journal of Microwave and Wireless Technologies

cambridge.org/mrf

Ka-band single-pole double-throw switch in GaN MMIC technology

Seyed Urman Ghozati and Roberto Quaglia

School of Engineering, Cardiff School of Engineering, Cardiff University, Queen's Buildings, Cardiff, Wales, United Kingdom

Research Paper

Cite this article: Ghozati SU, Quaglia R (2025) Ka-band single-pole double-throw switch in GaN MMIC technology. *International Journal of Microwave and Wireless Technologies* **17**(2), 202–212. https://doi.org/10.1017/S1759078725000108

Received: 13 June 2024
Revised: 15 January 2025
Accepted: 18 January 2025

Keywords:
GaN HEMT; load-pull measurements; mm-wave applications; single-pole double-throw; tunable reflective termination

Corresponding author:
Seyed Urman Ghozati;
Email: GhozatiSU@cardiff.ac.uk

Abstract

This work describes the design process of a single-pole double-throw (SPDT) microwave switch operating at Ka-band. It is tailored to a tunable reflective termination design that can be used in tunable power amplifier configurations. A high electron mobility transistor and a resonating network are employed in shunt configuration to enhance the performance in the output port's active and inactive conditions. The small and large signal measurements showcase a 2 GHz bandwidth with an insertion loss and isolation better than −1.8 dB and −25 dB, respectively, and handling power levels of up to 3 W at 30.5 GHz. The load-pull measurements across the entire Smith chart offer comprehensive insights into the behavior of the SPDT when operating with complex and reactive loads, fulfilling the purpose of tunable reactive termination.

Introduction

Field-effect transistors (FETs) have been utilized in microwave switching networks since the 1970s, pioneered by Gaspari and Yee [1]. Since then, continuous research efforts have focused on improving performance metrics such as reducing insertion loss in the on-state, robust isolation in the off-state, and increasing power handling capacity. These improvements target the switching element, such as FET-based active devices, and the associated passive networks to alter specific figures of merit, such as operating frequency. This progress is also driven by the need to maintain compatibility with further miniaturization trends facilitated by emerging compound semiconductor materials such as gallium nitride (GaN). However, despite these advances, it is challenging to find commercially available switches operating at the required frequency while meeting high-power handling requirements with acceptable insertion loss and isolation.

The orthogonal load-modulated balanced amplifier (OLMBA), as proposed in [2], highlights the pivotal role of the reactive component (denoted as jX) introduced at the isolated output port in the load modulation process. This reactive termination reflects the control signal power back into the balanced stages of the amplifier, thereby enabling effective load modulation. Since the optimal value of jX varies depending on the specific configuration of each OLMBA and remains unknown, a configurable switching network capable of alternating between various reactive loads enhances its functionality.

Therefore, we are driven to develop a single-pole double-throw (SPDT) operating at mm-wave frequencies aimed at creating a tunable reflective termination, serving as a component in future designs of OLMBAs. As depicted in Fig. 1, the primary purpose of employing an SPDT is to load with two different reflective loads, jX_1 and jX_2, which can be selected electronically. In the final application, the OLMBA's output isolated port will be connected to the SPDT's common input (RF_{in}), while the SPDT's output ports (RF_1 and RF_2) are loaded with suitable, fixed passive reactive components, such as capacitors, inductors, short or open circuits, or transmission lines. Due to the symmetry of the architecture, both ports can be taken under test for any loading conditions. Since the target values of jX_1 and jX_2 depend on the specific OLMBA configuration, the SPDT was designed to accommodate arbitrary reactive components and tested across a wide range of values using load-pull (LP) measurements to evaluate its performance. Various methodologies and design strategies can be utilized to create an SPDT [3, 4]. The operational concept of the SPDT involves a common input port (RF_{in}), with ports RF_1 and RF_2 as outputs. The SPDT operates in a symmetrical and complementary configuration, where one output is active (throw) while the other remains inactive (isolating). In the following sections, the design process of the SPDT, along with its key characteristics, will be thoroughly explained.

An earlier version of this work [5] investigated the FET-based switch cell in an OLMBA context, where behavioral model for the single high electron mobility transistor (HEMT) switch with 0.15 μm gate operating at 3 GHz, while this work presents the design and characterization of an SPDT switch operating at Ka-band, utilizing four HEMT structure switches, each with a 0.12 μm gate length.

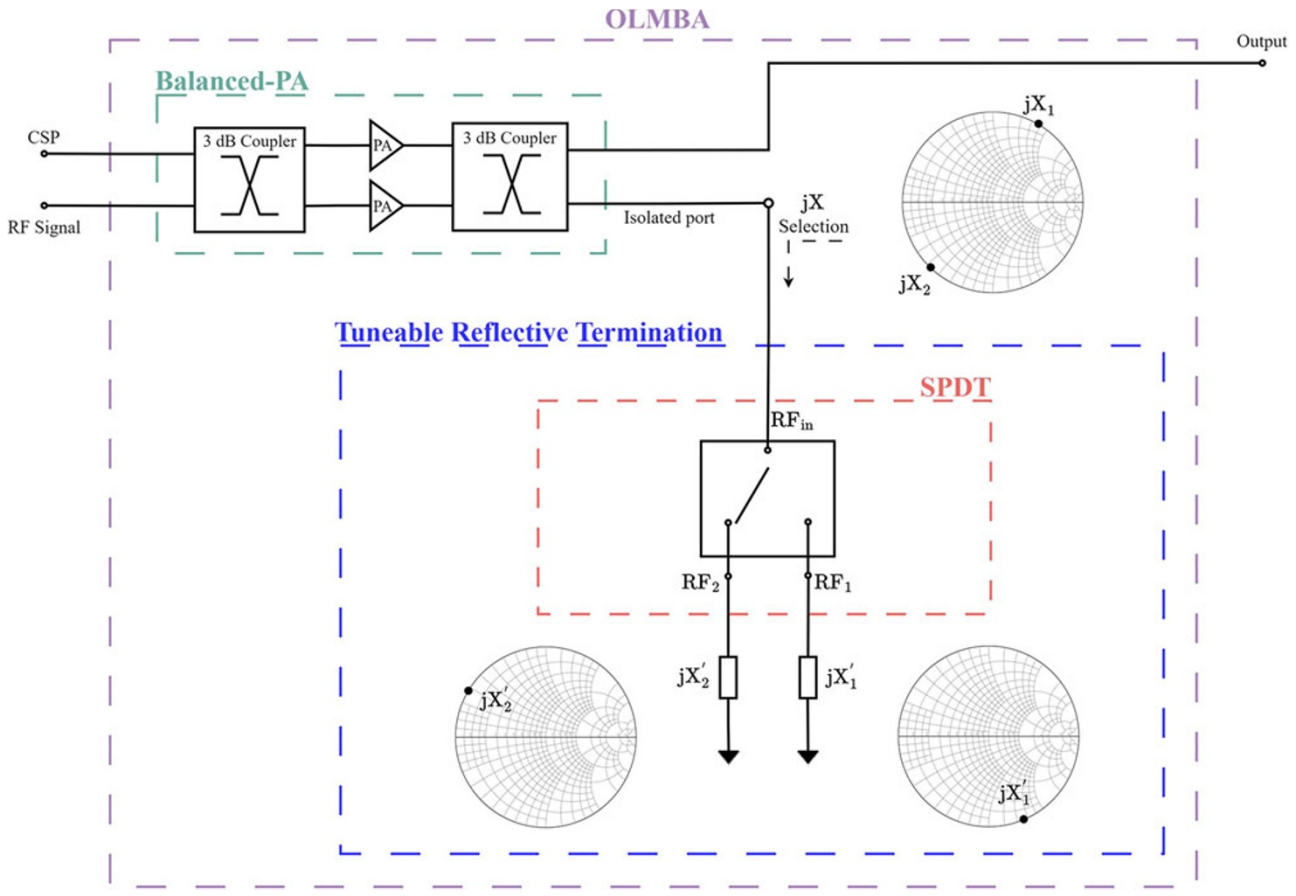

Figure 1. The orthogonal load modulated balanced amplifier with a tunable reflective termination employing an SPDT to be introduced to two different reactive loads of jX_1' and jX_2'.

Design process

Passive HEMT characterization

This paper employs the WIN Semiconductors NP12-01 GaN-on-SiC technology targeting mm-wave power applications. This 0.12 μm gate process is manufactured on 50 μm SiC substrates. It uses a source-coupled field plate design to provide the high breakdown voltage required for reliable operation at the drain bias of 28 V, showing a typical saturated output power of 4 W/mm and drain efficiency over 50% at 29 GHz. The NP12-01 platform supports multiple microwave monolithic integrated circuit (MMIC) functions, including optimized switch transistor layouts, two interconnect metal layers, high-reliability metal-insulator-metal (MIM) capacitors, precision TaN resistors, and through wafer's vias for low inductance grounding. While Fig. 2(a) shows a microphotograph of the switch cell, Fig. 2(c) presents a block diagram illustrating both its topology and biasing configuration.

The small signal performance of the switch cell is evaluated in terms of on-state insertion loss and off-state isolation, both calculated from the forward transmission coefficient (S_{21}) expressed in decibels (dB):

$$20\log_{10}(|S_{21}|)\begin{cases}\text{Insertion loss} & \textit{if ON}\\ \\ \text{Isolation} & \textit{if OFF}\end{cases}. \quad (1)$$

Figure 2(b) displays the measurement of the small signal scattering parameters of the device under both ON (0 V) and OFF (−30 V) conditions, covering the frequency range from 500 MHz to 40 GHz. While the device exhibits acceptable responses throughout the frequency spectrum during on-state, limitations arise during off-state, particularly at higher frequencies, primarily attributed to parasitic capacitance effects.

The widely accepted figure of merit (FoM) for switches known as cutoff frequency (F_c) is a product of low and high impedance during the ON and OFF conditions, respectively [6, 7]:

$$F_c = 1/(2\cdot\pi\cdot R_{on}\cdot C_{off}), \quad (2)$$

where

$$R_{on} = 2Z_0\left(10^{-\frac{S_{21}(\text{dB})}{20}}-1\right) \quad (3)$$

$$C_{off} = 1/2Z_0\left(\omega\cdot\sqrt{10^{-\frac{S_{21}(\text{dB})}{10}}-1}\right). \quad (4)$$

The F_c is a performance indicator rather than representing the actual operating frequency, and the rule of thumb suggests that the switch cell should be usable in designing microwave switches up to approximately $F_c/10$.

Table 1 provides a comparative analysis of the NP12 technology used in this work and the NP15 technology from the early version of this work [5]. This information provides insights into their F_c product, aiding in our decision to transition from NP15 to NP12, given the design frequency around 30 GHz.

https://doi.org/10.1017/S1759078725000108 Published online by Cambridge University Press

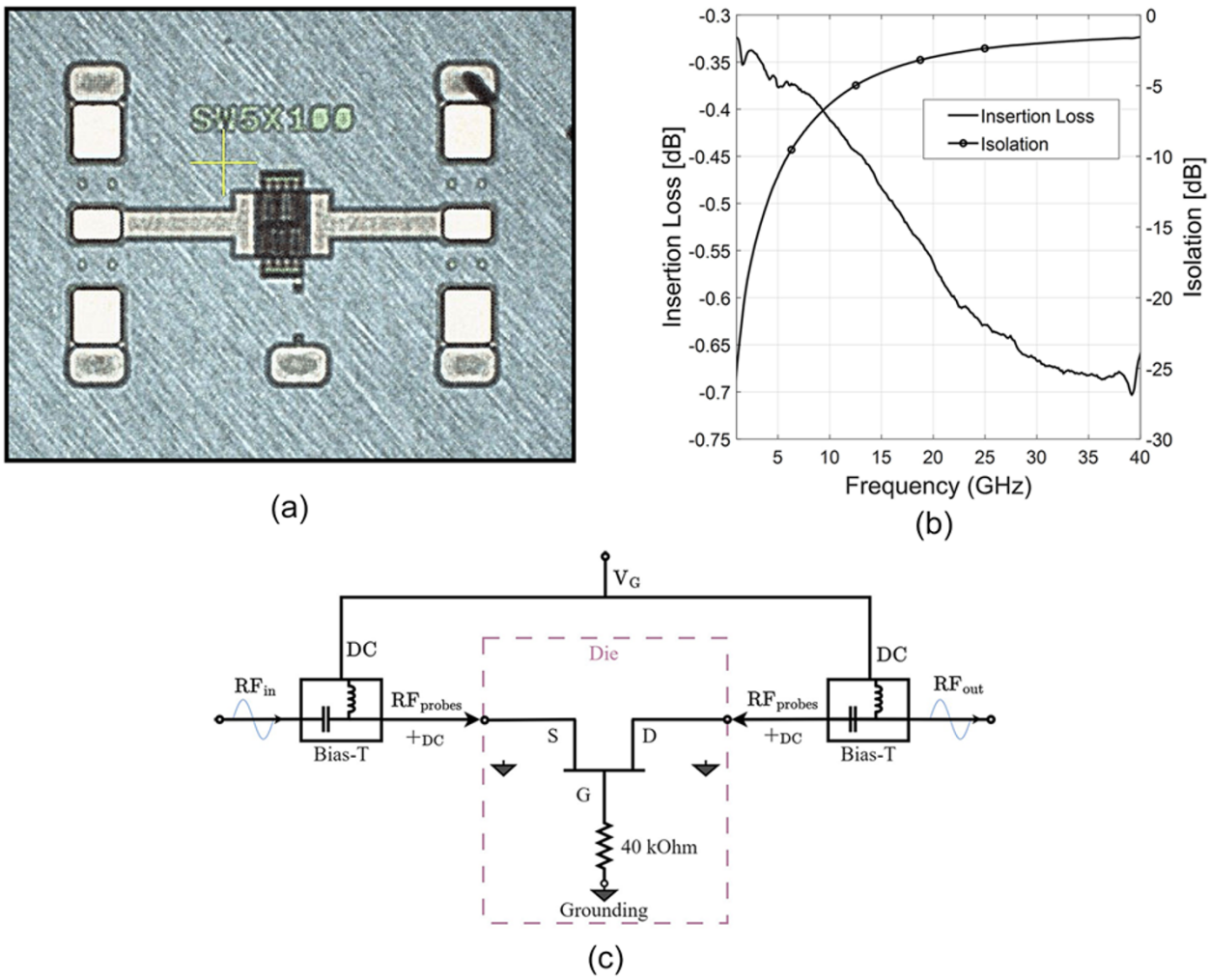

Figure 2. Microphotograph of a five-finger gate device with a 100 μm gate width using NP12 technology (a), circuit diagram and biasing configuration of the same device (b), device performance through small signal characterization (c).

Table 1. Comparison of simplified switch characteristics between the NP12 and NP15 technologies

Gate length (nm)	R_{on} (Ω)	C_{off} (fF)	F_c (GHz)
120 (NP12)	7.98	68	290
150 (NP15)	6.27	122	207

Small signal model

Due to the absence, at the time of the design, of a large signal model for the switch in the process design kit and considering the time constraints associated with generating a complete nonlinear model, the decision was made to proceed based on small signal measurements and an equivalent small signal model. The small signal model is developed based on proposed components and formulations by [8]. Figure 3(a) illustrates the equivalent circuit diagram of the model, which includes gate-to-source capacitance, gate-to-drain capacitance, and channel inductance (C_{sg}, C_{dg}, L_{ch}), all of which are known as common parasitic to both ON and OFF states. In the OFF state, a drain-source capacitance (C_{ds}) and in the ON state, a total drain-source resistance (R_{ds}) are introduced as core components to demonstrate high and low impedance conditions, respectively. It is important to note that although the common components remain the same, their values differ significantly between the ON and OFF modes. For model validation, the measured S-parameters are compared with the model responses depicted in Fig. 3. The application of small signal model during the design phase proved adequate, as the operating frequency remained below the device's cutoff frequency, ensuring linear behavior. Additionally, the switch is intended to function with minimal power impact, operating within the device's power limits as determined by the 1 dB compression point in the ON condition and achieving isolation better than −20 dB in the OFF state.

Switching network design

The effectiveness of shunt topology in switch design, particularly in regard to insertion loss, is widely acknowledged [9]. Therefore, a reflective shunt arrangement has been selected as illustrated in Fig. 4(a). The shunt leg would operate reciprocally to the port itself, while the device in the shunt leg is in the on-state, the port is in the inactive (isolating) mode, and vice versa.

Figure 4(b) depicts the transition of the impedance corresponding to the lowest measured frequency (500 MHz) to the

https://doi.org/10.1017/S1759078725000108 Published online by Cambridge University Press

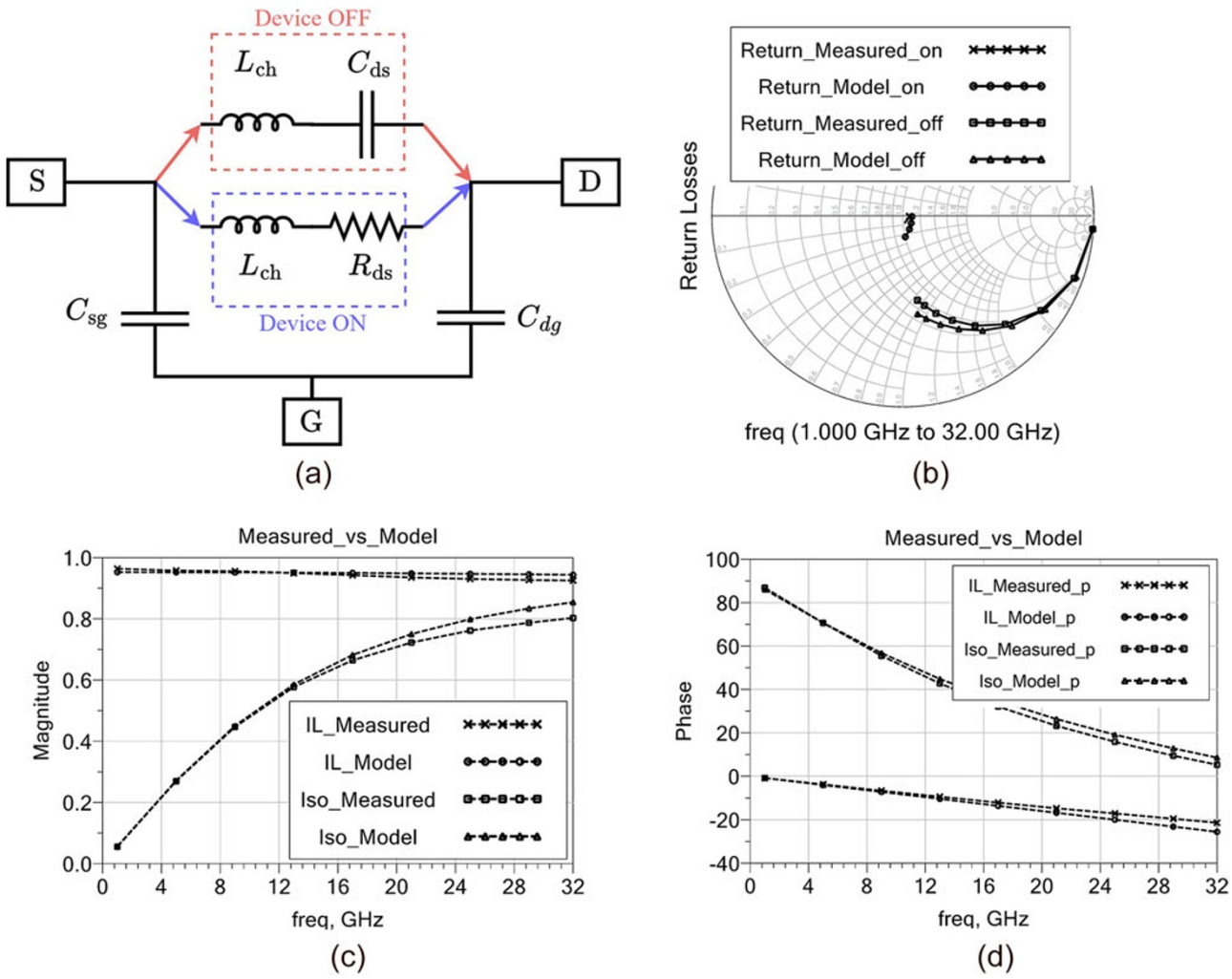

Figure 3. Simplified small signal model components for both ON and OFF conditions (a), return losses for both ON and OFF conditions (b), model and measured response comparison; magnitude of forward transmission (c), phase of forward transmission (d).

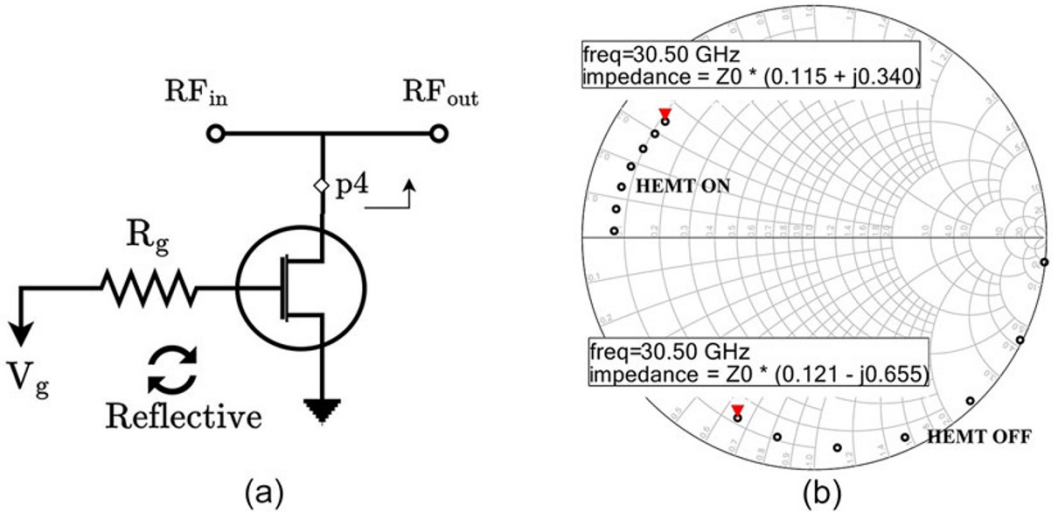

Figure 4. Reflective topology of the stand-alone shunt (a), measured device impedance transformation from low frequency to 30.5 GHz under both ON and OFF conditions ($Z0 = 50\Omega$) (b).

https://doi.org/10.1017/S1759078725000108 Published online by Cambridge University Press

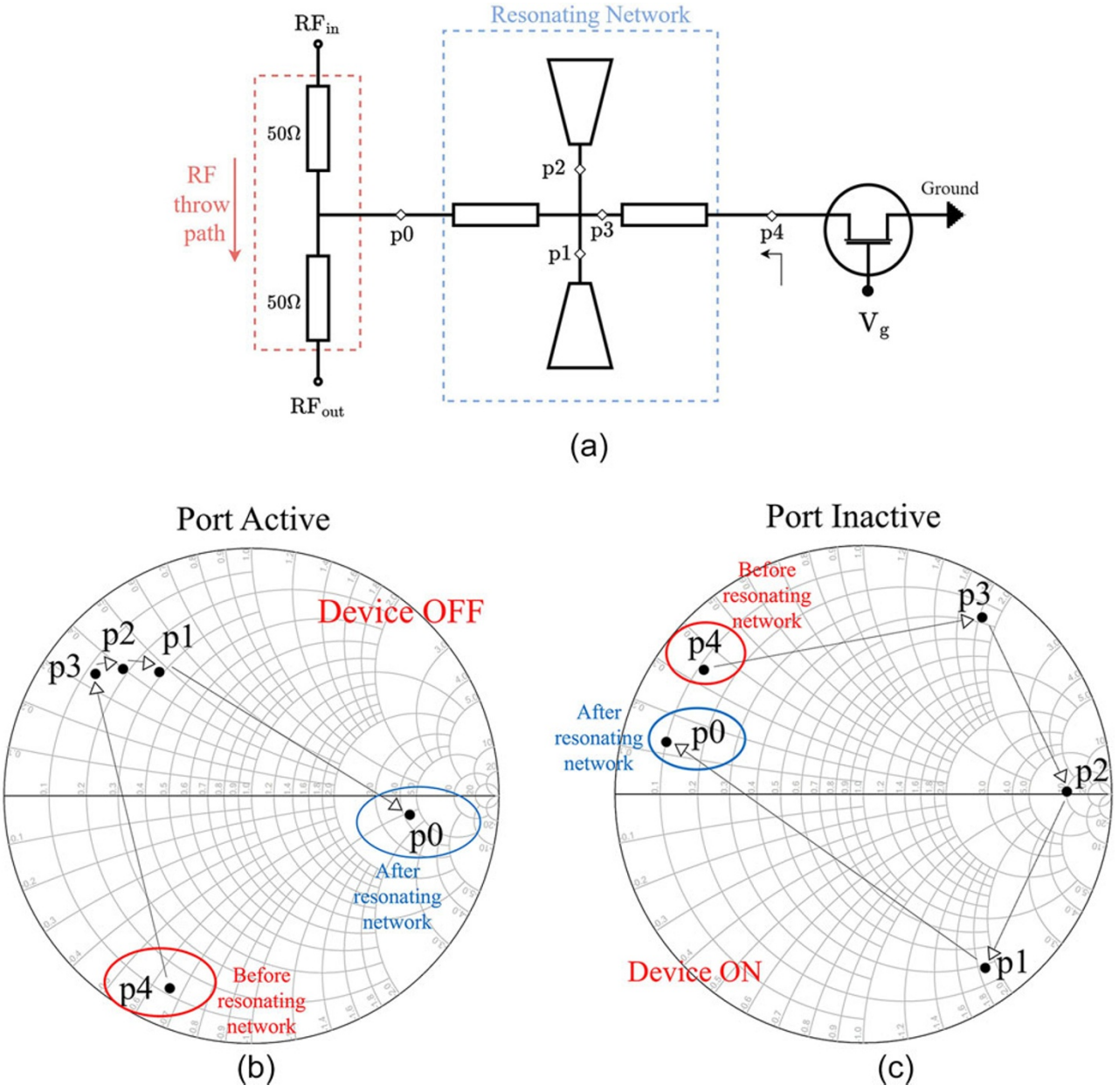

Figure 5. Resonating network preceding the passive HEMT device (a), passive HEMT impedance transformation at 30.5 GHz: port active (b), port inactive (c).

impedance corresponding to the highest measured frequency (30.5 GHz) under the ON and OFF conditions. The device in the on-condition (port inactive) maintains an acceptable low impedance ($\approx (0.115 + j0.34)Z_0$) peaking at 30.5 GHz. However, during the devices' off-condition (port active), a significant deviation occurs, transitioning from a high impedance condition (near open circuit) at lower frequencies to a considerably lower impedance ($\approx (0.121 - j0.655)Z_0$) when approaching 30.5 GHz.

This degradation in performance under stand-alone configurations at higher frequencies motivated further exploration into impedance transformation techniques. Incorporating a resonating network into the shunt leg preceding the passive HEMT device (in contrast to [10] where the resonating component was in parallel with the passive FET device) showed promising results in simulations. As illustrated in Fig. 5(a), the network comprises a series transmission line connected to two parallel tapered open circuit stubs, providing an equivalent shunt capacitance in series with another high-impedance line. In contrast to the impedance transformation network presented in [11], which converts a low impedance to a high impedance and vice versa, the resonating network presented in this work is designed to optimize the impedance with the aim of a lower impedance (near short) during the ON condition of the devices (port inactive) and high impedance (near open) during the OFF condition of the devices (port active) throughout the spectrum of frequencies with consistent physical geometry.

At the design frequency (30.5 GHz) when the output port is in the active condition, the device which is biased with −30 V (device OFF) shows the impedance at the point p4 in Fig. 5(b). The resonating network transforms the impedance from p4 to p0, ensuring that

https://doi.org/10.1017/S1759078725000108 Published online by Cambridge University Press

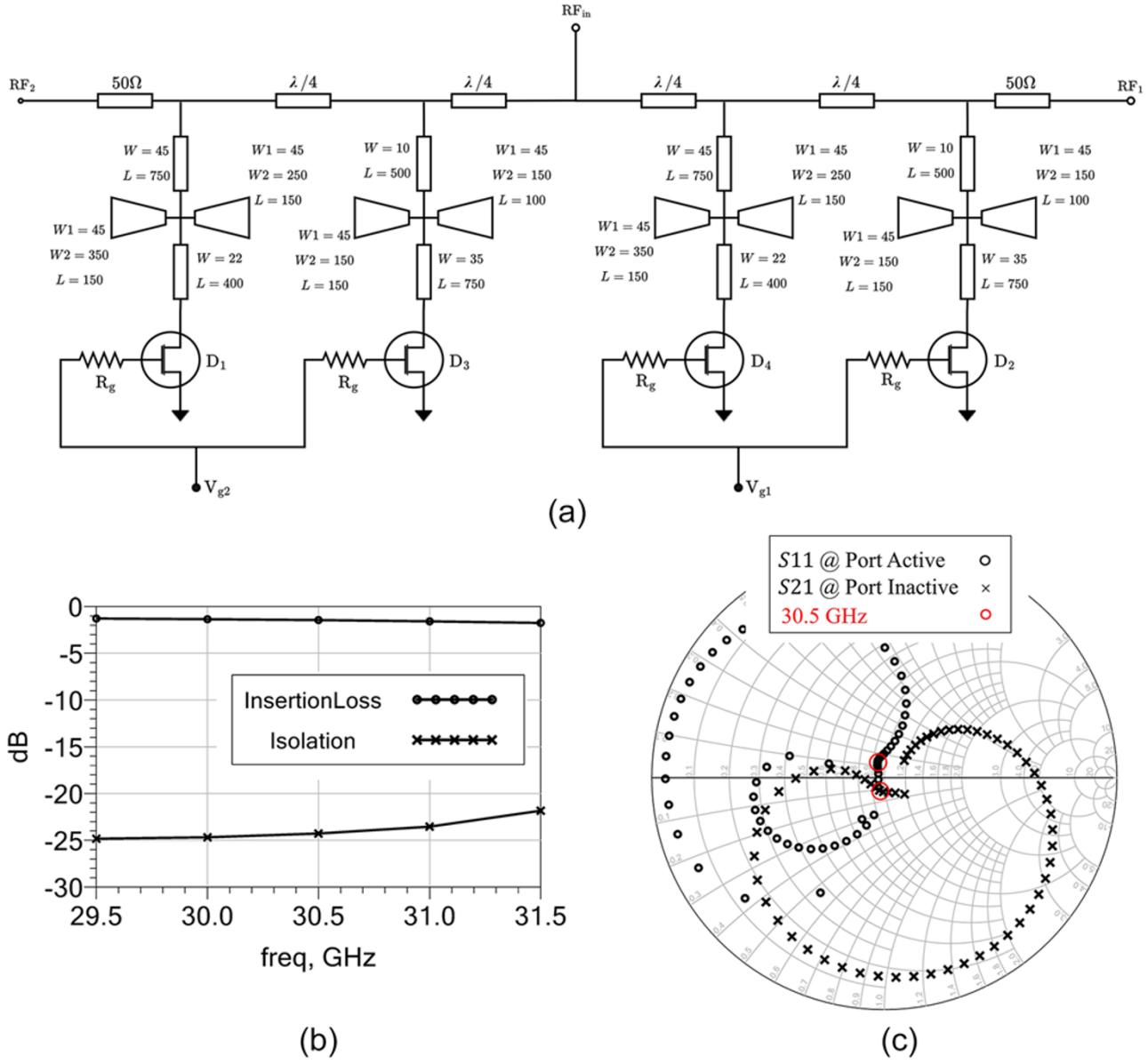

Figure 6. Detailed schematic of the SPDT (a), insertion loss and isolation versus frequency (b), loss parameters (c).

the traveling signal encounters an impedance closer to the open circuit at junction p0 in Fig. 5(a). In contrast, when the output port is inactive the device is biased with 0 V (device ON), resulting in a low impedance with inductive behavior at point p4 in Fig. 5(c), the resonating network facilitates the transformation from p4 to p0, ensuring that the traveling signal encounters a short circuit at junction p0 in Fig. 5(a) and directed toward the source via ground.

The tapered open-circuit stubs apply minimal impact during the HEMT off-state (port active), as their capacitive reactance is relatively insignificant compared to the drain-to-source capacitance of the passive HEMT in off-condition. However, their significance becomes more pronounced during the HEMT on-state (port inactive), which is crucial in transforming the impedance toward a point near-short.

The resonating network shown in Fig. 5(a) compensated for the degradation of the HEMT device in switching operations at the design frequency. The same topology was duplicated and connected to a common node through quarter-wavelength transmission lines to form an SPDT. Initially, each arm of the SPDT included a single resonating network. However, during optimization, it was discovered that a better bandwidth response could be achieved by utilizing two resonating networks in parallel, interconnected by quarter-wavelength transmission lines, as depicted in Fig. 6(a), which shows the detailed schematic of the SPDT with two shunt resonating networks at each arm. Each resonating network was independently optimized during the layout transformation. The symmetrical topology of the SPDT simplifies the measurement process, as a single arm can be tested for both active and inactive conditions.

Circuit-level simulation, performed using the completed layout of the SPDT with values detailed in Fig. 6(a), confirms an insertion loss of better than −1.7 dB and isolation below −20 dB for a 2 GHz bandwidth, as illustrated in Fig. 6(b). The results obtained indicate

https://doi.org/10.1017/S1759078725000108 Published online by Cambridge University Press

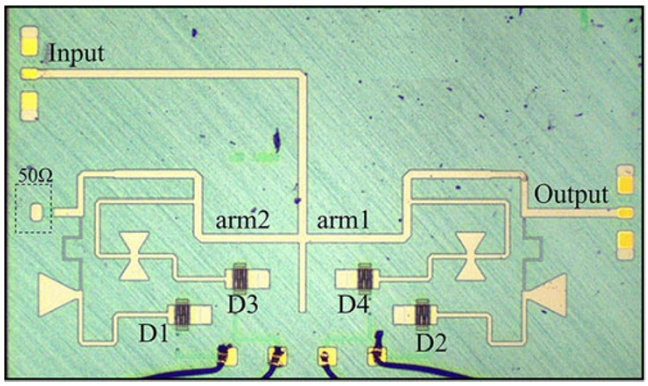

Figure 7. Microphotograph of the SPDT switch. The size, without additional lines for testing ≈ 3.1 × 1.0 mm², with access lines ≈ 3.1 × 1.8 mm².

the potential to extend the bandwidth via isolation enhancement, possibly at the expense of a modest increase in insertion loss. As depicted in Fig. 6(c), the reflection coefficients (S_{11}) when the output port is active, alongside the forward transmission (S_{21}) during the output port's inactive state, offer valuable insight attributed to the matching and associated losses.

As shown in the microphotograph of the final layout in Fig. 7, an additional transmission line was added at the common node to address probe positioning constraints in the measurement system. To minimize chip area, the transmission lines were reshaped, with electromagnetic simulations applied to ensure design performance within the desired response range.

In order to test under two-port measurement system conditions, the RF input and output (arm1) are equipped with RF and DC pads, while arm2 is terminated with an integrated 50Ω resistor. This setup requires arm1 to be tested for both port's active and inactive conditions. However, HEMT devices in arm2 will still be biased complementary to arm1. When the port under test (arm1) is in the active state, D2 and D4 devices will be supplied with −30 V to maximize transmission, while D1 and D3 devices will be biased with 0 V to minimize reflection by diverting signals to the source via ground. The opposite biasing arrangement will be applied for the port-inactive scenario.

Measurement

Small and large signal measurement

As depicted in Fig. 8(a), in order to prepare the test fixture, the SPDT die is mounted on a 5 mm thick aluminum base plate to assist with heat dissipation. An external PCB is also mounted on the same base plate to provide biasing to the MMIC. Although the devices are intended to be equally biased in pairs, four distinct launchers have been incorporated to increase flexibility for potential future tuning requirements. The wire bonding was performed using 25 μm thick gold wires to connect the MMIC to the PCB. Four high-frequency ceramic capacitors (100 pF/100 V) were positioned between the die and each launcher on the PCB. This arrangement simplifies the bond wiring process from the millimeter scale of the MMIC to the PCB's centimeter scale, and also provides filtering of the DC bias.

The measurement system set up to characterize small signal behavior uses a PNA Network Analyzer N5227B from the Keysight and MPI GSG 150 μm probes as depicted in Fig. 8(b). To compensate for the systematic errors introduced by measurement system components and to establish accurate reference standards, the measurement system is calibrated by performing a TRL (thru-reflect-line) calibration using a calibration kit on the same substrate.

As illustrated in Fig. 9(a), the achieved performance metrics ensure an insertion loss of better than −1.8 dB and isolation below −25 dB across a 2 GHz bandwidth around the center frequency of 30.5 GHz, under the active and inactive conditions, respectively.

In large signal measurement, the first step is to conduct a power sweep with the load fixed at 50Ω. To achieve saturation of the device at 30.5 GHz, a pre-amplifier (Spacek Labs SP313-35-38) and a power amplifier (Qorvo QPA2211B) were employed at the input. The SPDTs' power handling has been determined by the input power corresponding to a maximum power gain compression of 0.1 dB in the active state and a maximum reflection coefficient magnitude of −20 dB in the inactive mode.

To analyze the port in its active mode, the power gain was selected as the FoM to demonstrate the insertion loss and the compression over the sweeping rang at the design frequency. The power gain parameter is calculated from the extracted traveling wave components (a_1, a_2, b_1, and b_2). Figure 9(b) demonstrates that the SPDT maintains a low loss at power levels of up to 3 W, delivering a power gain better than −2 dB. In port's inactive mode, the magnitude of the input reflection coefficients was selected as the FoM to represent the isolation capability of the SDPT under large signal characterization. Figure 9(b) shows the captured $|\Gamma_{IN}|$ responses remain below −20 dB for applied power levels of up to 2 W. It is evident in Table 2 that published SPDT devices often compromise specific figures of merit to improve other parameters. In contrast, the SPDT device developed in this study demonstrates consistently high performance across all evaluated metrics

$$\text{Power Gain [dB]} = P_{\text{out}}\,[\text{dBm}] - P_{\text{inDel}}\,[\text{dBm}]. \tag{5}$$

LP measurement

The main goal of this study is to develop a switching network capable of effectively connecting with reactive components to ensure the best possible operation of OLMBAs. To achieve this objective, a low-loss SPDT was designed, fabricated, and tested at the specified frequency, meeting the necessary operating power level requirements. As discussed previously, due to the use of a two-port measurement system, one port of the SPDT was terminated with a 50Ω load during the design phase, leaving only one remaining port available for the connection to reactive components. Since the specific reactive terminations for the OLMBA were not known at the time of design, manual testing of iterations proved inefficient. Consequently, LP measurements were utilized as a comprehensive method to simulate a wide range of reactive terminations and record the SPDT's response under varying load conditions. This approach offers valuable insights into the SPDT performance across the entire Smith chart when exposed to capacitive or inductive loads.

Figure 10 depicts the employed passive LP measurement system and its block diagram with PNA-X Network Analyzer N5247B from Keysight, passive on-wafer Delta M67100 tuner from focus, and MPI's 150 μm GSG (T67A) probes. The passive tuner is programmed to define 136 unique loads, including the 50Ω, with 6 magnitudes arranged in a circular pattern across the Smith chart.

https://doi.org/10.1017/S1759078725000108 Published online by Cambridge University Press

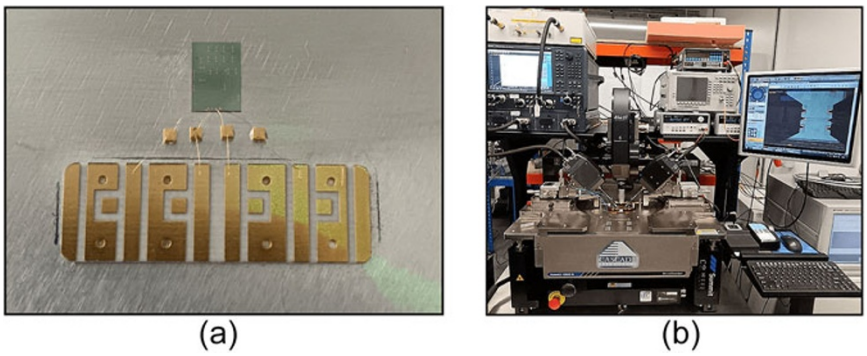

Figure 8. SPDT test fixture (a), small signal measurement system (b).

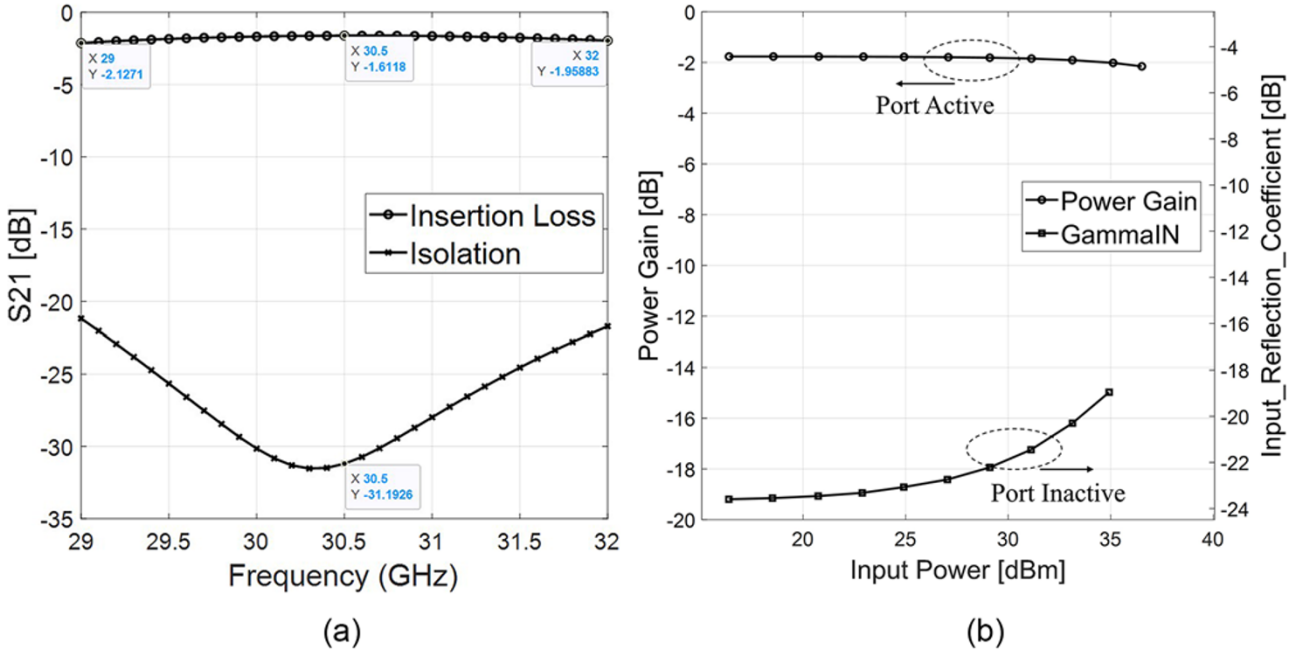

Figure 9. Insertion loss and isolation versus frequency (a), power gain and input reflection coefficient versus input power in port's active and inactive conditions (b).

Table 2. Comparison of the designed MMIC with published GaN MMIC SPDTs

Ref.	Freq (GHz)	Isolation [dB]	Insertion Loss [dB]	Return Loss [dB]	0.1P [dBm]	Chip size (mm^2)
[12]	8.4–10.8	< -20	> -1.2	< -10	38	3.0×1.5
[13]	8–12	< -40	> -2	NA	25	3.2×1.2
[14]	0–12	< -12	> -1	< -12	35	1.2×1.7
[15]	27–31	< -25	> -1.3	NA	41	1.7×0.9
[16]	26–30	< -37	> -1.5	< -15	48	3.7×0.5
[17]	8–12	< -28	> -5	< -8	44	4.0×1.8
This work	29.5–31.5	< -25	> -1.8	< -8	37	3.1×1.8

Figure 11 shows the reflection coefficient measured at the input of the SPDT (Γ_{IN}, blue circles) when load-pulling, while black circles correspond to the output loads set (Γ_L), for the swept input powers at 30.5 GHz. Figure 11(a) shows the case where the SPDT is switched to RF_2, which means that the RF_1 port (arm1) is in inactive condition. In this mode, ideally, load-pulling the RF_1 port should not have any effect on Γ_{IN} as RF_1 is isolated from the input. Figure 11(a) confirms this as it shows a 50Ω at all power levels for all defined output loads (Γ_L). Such a response originates from arm2 being terminated at 50Ω. The slight mismatches of captured Γ_{IN}s and the 50Ω attributes to the loss associated with the network. This provides additional information compared to what presented in Fig. 9(b) to demonstrate the SPDT's high isolation capability.

Figure 11(b) shows the results for the port's active condition. The insertion loss of the switch leads to a reduction in the magnitude of the reflection coefficient, which can be achieved at the input of the switch. In addition, the response is asymmetrical, with the highest magnitude achieved for low inductive impedances.

https://doi.org/10.1017/S1759078725000108 Published online by Cambridge University Press

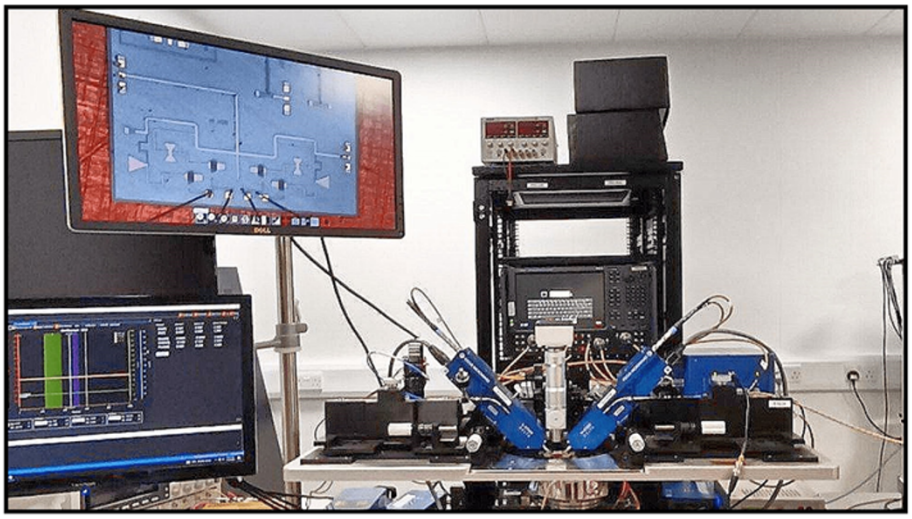

(a)

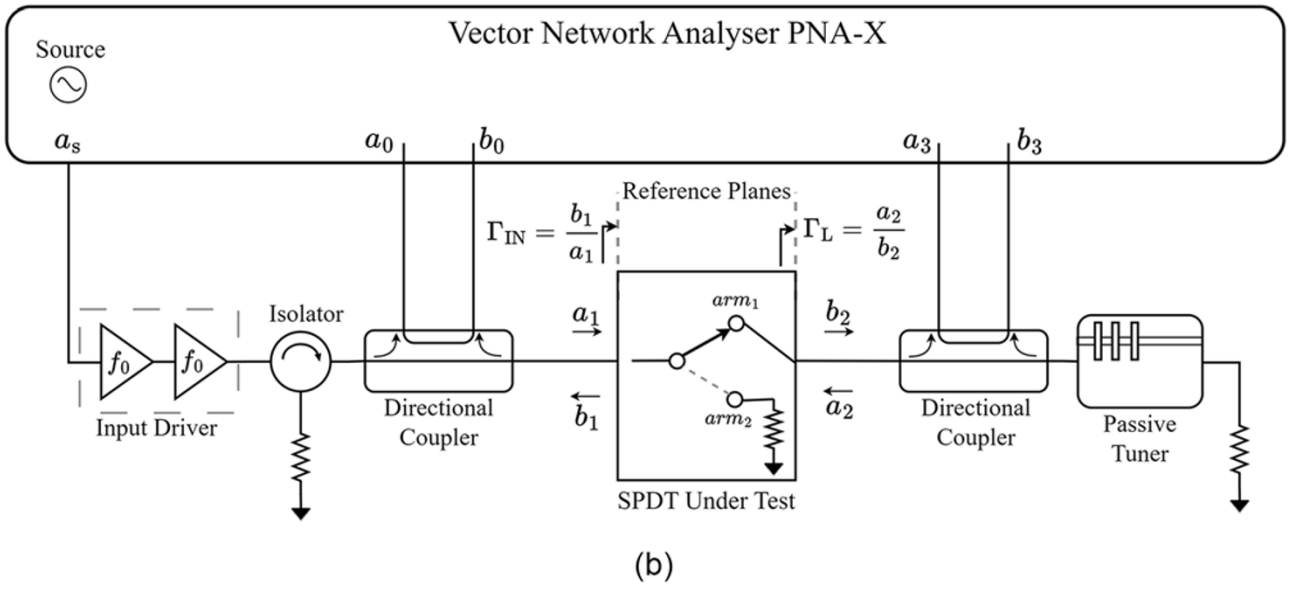

(b)

Figure 10. The passive load-pull measurement system at CSA Catapult (a), the block diagram of the same system (b).

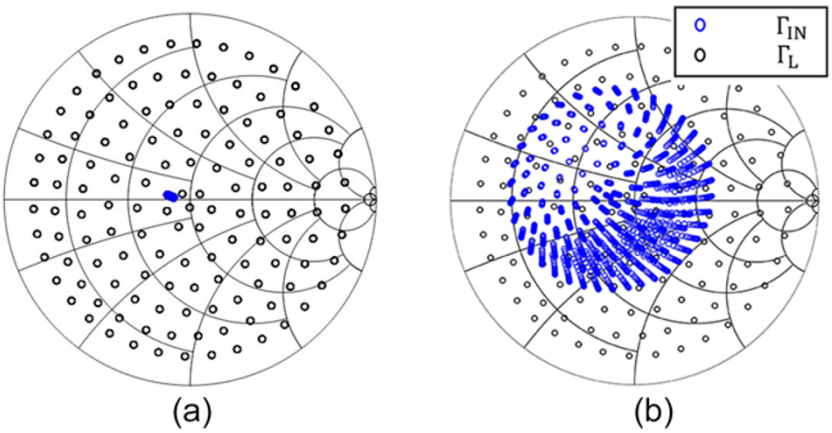

(a) (b)

Figure 11. Γ_{IN} (blue circles) versus Γ_L (black circles) included with power sweeps for port's inactive condition (a), port's active condition (b).

https://doi.org/10.1017/S1759078725000108 Published online by Cambridge University Press

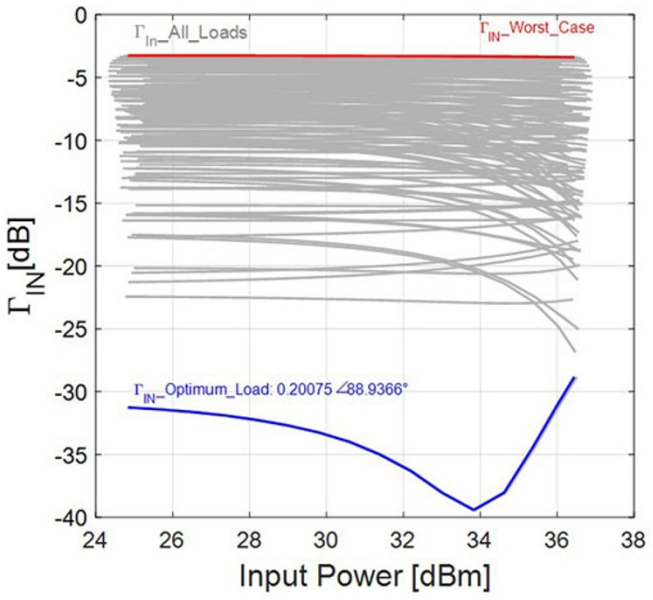

Figure 12. Γ_{IN} variations at different power levels with various loads.

The worst case is the capacities of the fourth quadrant in the Smith chart, which also exhibits the most significant variations versus power sweep, which can also be observed in Fig. 12 where the magnitude of Γ_{IN} is shown versus the input power for all the loads tested. Figure 11(b) expresses the challenges associated with the introduction of purely reactive components, recapturing the jX_1 with the same characteristics and the number of potential iterations required to determine the optimal jX. The position in the Smith chart of the best and worst loading can be arbitrarily changed by adjusting the length of the input line. The asymmetry in the SPDT response can be attributed to the asymmetric behavior of the elemental switch, as discussed in [5]. The abovementioned underscores the importance of LP data. Moreover, the LP data will be leveraged in future work to develop a comprehensive large-signal model of the tested SPDT. This model will be pivotal in optimizing the final OLMBA design within computer-aided design tools, ensuring accurate performance prediction under real-world operating conditions.

Conclusion

This study presents an SPDT featuring an insertion loss of −1.8 dB and isolation exceeding −25 dB, maintaining linearity up to 3 W for the center frequency of 30.5 GHz. While the designed SPDT demonstrates the capability to function in conventional applications, such as Tx/Rx switching, its primary purpose was to enable the creation of a tunable reflective termination by enabling switching between various reactive loads. An LP measurement was conducted to capture the SPDT's response to a wide range of reactive loads across the entire Smith chart, providing valuable insight into the variations of the loss and distortion that occur when changing the load. In future work, we will utilize the LP data to generate a large signal behavioral model of the fabricated SPDT. This model will enable us to simulate the SPDT within the design process of an OLMBA.

Acknowledgements. The authors would like to thank WIN Semiconductors Corp. for fabricating the SPDT, CSA Catapult and Dr. Ehsan Mehrabi Azad for providing the measurement system, and Alexander Baddeley for his assistance in the measurement process.

Competing interests. The authors report no conflict of interest.

References

1. **Gaspari R and Yee H** (1978) Microwave GaAs FET switching. In *IEEE-MTT-S International Microwave Symposium Digest*. Ottawa: IEEE, pp. 58–60.
2. **Collins DJ, Quaglia R, Powell JR and Cripps SC** (2020) The orthogonal LMBA: A novel RFPA architecture with broadband reconfigurability. *IEEE Microwave and Wireless Components Letters* **30**, 888–891.
3. **McLevige W and Sokolov V** (1981) Resonated GaAs FET devices for microwave switching. *IEEE Transactions on Electron Devices* **28**, 198–204.
4. **Tajima Y, Titus W, Mozzi R and Morris A** (1984) Broadband GaAs FET 2 × 1 switches. In *IEEE GaAs IC Symposium Technical Digest*. Boston: IEEE, pp. 081–084.
5. **Ghozati SU, Quaglia R, Azad E, Powell J, Tasker P and Cripps S** (2023) Load pull-driven behavioral modelling of microwave switches for the design of tunable reflective terminations. In *2023 18th European Microwave Integrated Circuits Conference (EuMIC)*. Berlin: IEEE, pp. 1–4.
6. **Drozdovski N and Caverly R** (2002) GaN-based high electron-mobility transistors for microwave and RF control applications. *IEEE Transactions on Microwave Theory and Techniques* **50**, 4–8.
7. **Campbell CF, Dumka DC and Kao M-Y** (2009) Design considerations for GaN based MMICs. In *2009 IEEE International Conference on Microwaves, Communications, Antennas and Electronics Systems*. Tel Aviv: IEEE, pp. 1–8.
8. **Ehoud A, Dunleavy L, Lazar S and Branson R** (1995) Extraction techniques for FET switch modeling. *IEEE Transactions on Microwave Theory and Techniques* **43**, 1863–1868.
9. **Schindler M and Morris A** (1987) DC-40 GHz and 20-40 GHz MMIC SPDT switches. *IEEE Transactions on Microwave Theory and Techniques* **35**, 1486–1493.
10. **Lan G, Dunn D, Chen J, Pao C and Wang D** (1988) A high performance V-band monolithic FET transmit-receive switch. In *IEEE 1988 Microwave and Millimeter-Wave Monolithic Circuits Symposium. Digest of Papers*. New York: IEEE, pp. 99–101.
11. **Lin K-Y, Wang Y-J, Niu D-C and Wang H** (2003) Millimeter-wave MMIC single-pole-double-throw passive HEMT switches using impedance-transformation networks. *IEEE Transactions on Microwave Theory and Techniques* **51**, 1076–1085.
12. **D'Angelo S, Biondi A, Scappaviva F, Resca D and Monaco VA** (2016) A GaN MMIC chipset suitable for integration in future X-band space-borne radar T/R module frontends. In *2016 21st International Conference on Microwave, Radar and Wireless Communications (MIKON)*. Krakow: IEEE, pp. 1–4.
13. **Bettidi A, Cetronio A, De Dominicis M, Giolo G, Lanzieri C, Manna A, Peroni M, Proietti C and Romanini P** (2008) High power GaN-HEMT microwave switches for X-band and wideband applications. In *2008 IEEE Radio Frequency Integrated Circuits Symposium*, pp. 329–332.
14. **Campbell CF and Dumka DC** (2010) Wideband high power GaN on SiC SPDT switch MMICs. In *2010 IEEE MTT-S International Microwave Symposium*. Anaheim: IEEE, pp. 145–148.
15. **Zheng X, Tremblay JC, Huettner SE, Ip KP, Papale T and Lange KL** (2013) Ka-band high power GaN SPDT switch MMIC. In *2013 IEEE Compound Semiconductor Integrated Circuit Symposium (CSICS)*. Monterey: IEEE, pp. 1–5.
16. **Kim T, Im H, Lee S-H, Kim K-J and Park C** (2022) Highly linear K-/Ka-band SPDT switch based on traveling-wave concept in a 150-nm GaN pHEMT process. *IEEE Microwave and Wireless Components Letters* **32**, 987–990.
17. **Janssen J, Hilton KP, Maclean JO, Wallis DJ, Powell J, Uren M, Martin T, van Heijningen M and van Vliet F** (2008) X-Band GaN SPDT MMIC with over 25 watt linear power handling. In *2008 European Microwave Integrated Circuit Conference*. Amsterdam: IEEE, pp. 190–193.

https://doi.org/10.1017/S1759078725000108 Published online by Cambridge University Press

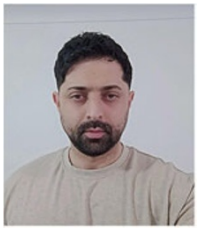

Seyed Urman Ghozati received his B.Eng. degree in Electronics and his first M.Sc. degree in Electrical Power Engineering from Northumbria University, Newcastle, in 2018. He then earned a second M.Sc. degree in Compound Semiconductor Electronics from Cardiff University in 2020, where he completed his Ph.D. with the Centre for High Frequency Engineering (CHFE). His research focuses on MMIC design, characterization, and modeling. He also has extensive hands-on experience in GaN technology fabrication, including RF active low and high-power devices.

Roberto Quaglia was born in Casale Monferrato, Italy, in 1984. He received the Ph.D. degree in electronic devices from Politecnico di Turin, Turin, Italy, in 2012. He is currently a Senior Lecturer with the School of Engineering, Cardiff University, Cardiff, U.K. His research interests include concern the design, modeling, and predistortion of high-efficiency microwave monolithic integrated circuit (MMIC) power amplifiers. Dr. Quaglia received the European Union Marie Skodowska Curie Fellowship in 2015, the 2009 Young Graduated Research Fellowship presented by the GAAS Association, and the 2024 IEEE Microwave Magazine Best Paper Award. He is the Deputy Chair of the IEEE MTT-TC 12.

https://doi.org/10.1017/S1759078725000108 Published online by Cambridge University Press